QUANTIFYING THE EFFECTS OF SHEAR STRAIN ON MELT DISTRIBUTION AND PERMEABILITY

Adaire Nehring

Dr. Wenlu Zhu and James Bader

GEOL394

28 April 2020

Abstract

Rate of melt ascent beneath mid-ocean ridges is controlled by the permeability of the partially molten regions of the upper mantle. Geochemistry data of mid-ocean ridge basalt (MORB) and observed dunite bodies in ophiolite suggest that magma transport is through a network of high porosity channels. High porosity melt channels can be either stress- or reaction-driven. To date, there is little quantitative constraint of the permeability of channelized melt networks. In this study, I will quantify the 3-dimensional (3D) melt distribution and permeability of sheared olivine basalt aggregates containing stress-driven melt-rich bands. I will test and apply various image analysis tools on the X-ray synchrotron microtomography images of the experimental charges to obtain the 3D melt distribution. I will use the 3D melt distribution to form the digital rocks and conduct virtual flow through experiments to calculate their permeability. Quantitative characterization of 3D melt distribution and permeability of sheared partially molten rock will provide much needed constraints on channelized melt transport of partially molten regions beneath ocean ridges.

Table of Contents

1. Introduction

At mid-ocean ridges, divergent plates in the lithosphere cause mantle upwelling and induce partial melting of underlying mantle peridotite (Fig. 1). Given that melt is less dense than the surrounding mantle, the melt will separate from the solid and move to the surface by porous flow (Kelemen et al., 1997). This transportation of melt is responsible for the production of new oceanic crust. The transport rate, which will affect the geochemistry and geophysical processes in partially molten regions, depends on the permeability of the partially molten region and the melt migration type. These types of migration may include porous flow through grain-scale networks (Miller et al., 2015), or channelized flow through melt conduits or fractures (Richardson et al., 1996).

Geochemistry data of mid-ocean ridge basalts (MORB) show that melt composition and uppermost mantle peridotite are at a chemical disequilibrium. This suggests that the melt ascension is likely through high-flux conduits that are chemically isolated from the surrounding mantle (Spiegelman and Kenyon 1992). For channelized melt transportation to occur, small amounts of melt must first segregate from the partially molten rock. If a positive feedback is present, these melt pockets can develop into melt-rich conduits that dominate magma transport. Such positive feedback can be either reaction-driven (i.e., Kelemen et al., 1997) or stress-driven (i.e., Holtzman et al., 2003).

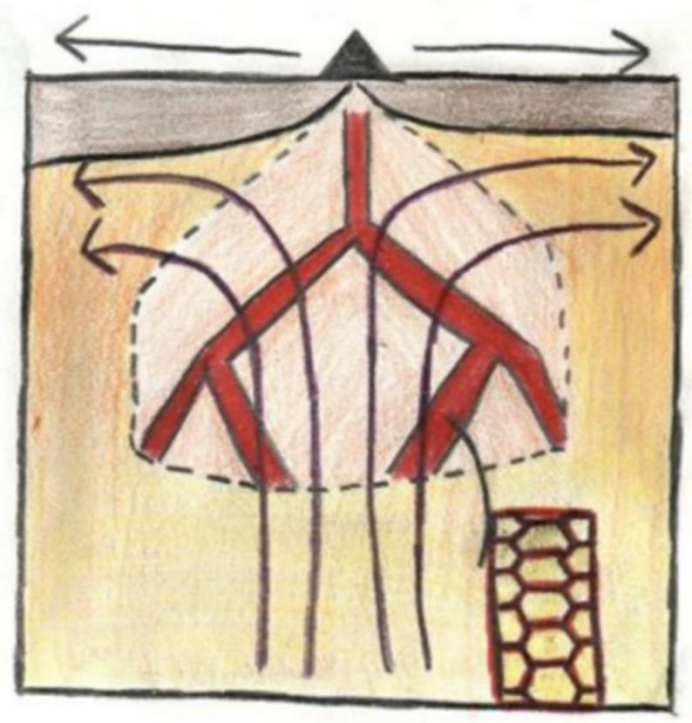

Fig. 1: *Diagram of a symmetrical spreading mid-ocean ridge. Arrows on surface indicate the direction of spreading. Curved arrows denote the direction of upwelling in the mantle. The red lines illustrate the channelization. Pop-out figure is an ideal grain-size melt geometry illustration. Image based off Miller et al., (2015).*

Stress-driven melt channelization has been observed in sheared partially molten olivine-basalt systems (Zimmerman et al., 1999). Figure 2 shows a network of melt-rich bands forming in sheared partially molten samples (King et al., 2009).

It has been observed that under high-pressure and high-temperature conditions, melt migration will occur under applied stress, and heterogeneous melt distribution will develop in the partially molten systems (Kohlstedt and Zimmerman 1996). The permeability of partially molten rocks containing melt-rich bands (e.g., Holtzman et al., 2003) is expected to be different from the isotropic systems (e.g., Miller et al., 2014). The permeability of partially molten rocks with channelized melt topology has yet to be quantified. Characterizing the permeability of sheared partially molten rocks that contains melt-rich bands will lead to a better understanding on melt transport beneath the mid-ocean ridges.

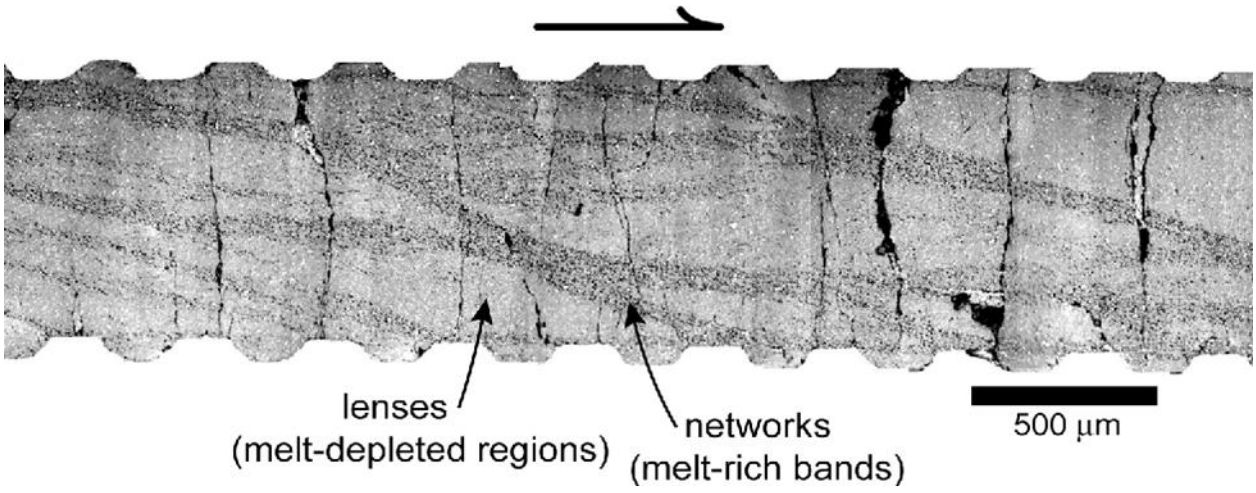

Fig. 2: *Olivine-basalt sample deformed in simple shear. Example of melt-poor (melt-depleted) and melt-rich regions from stress driven melt segregation. Melt-rich bands are dark, while melt-poor regions are light. Source: Kohlstedt and Holtzman (2009).*

2. Background

In an isotropic and homogeneous system consisting of a solid phase (e.g., olivine) and a liquid (e.g., melt), melt mainly resides in triple junctions (Zhu et al., 2011). Triple junctions are sections where three grains meet. At the solid-liquid boundary, the dihedral angle can be measured to assess the degree of connectivity (Bulau et al., 1979). When a dihedral angle is greater than 60°, melt pockets are usually disconnected from each other (e.g., Smith, 1964). When the dihedral angle is less than 60°, the melt will form interconnected networks along the grain edges (e.g., Smith, 1964; von Bargen and Waff, 1986). These factors determine the melt geometry and melt interconnectivity (Fig. 1) that will determine the permeability of the partially molten rocks.

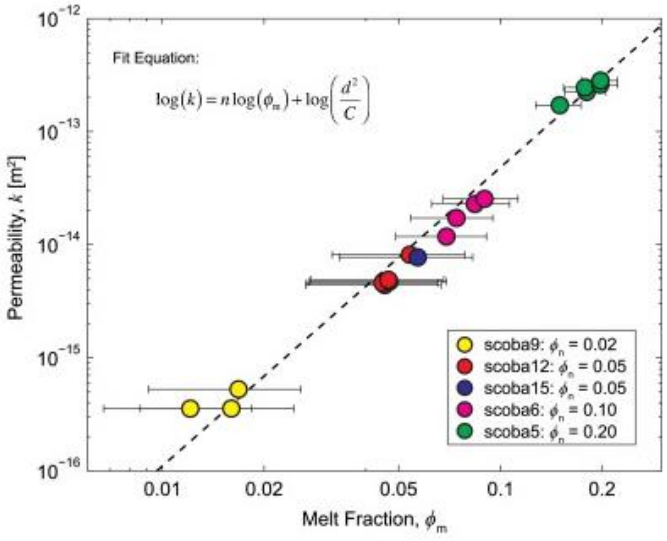

Fig. 3: *Relationship between melt fraction in calculated permeability as a function of measured melt fraction. As melt fraction increases, the permeability also increases. Data to quantify the relationship was experimented in olivine-basalt scoba samples. Dashed line is line of best-fit from the fit equation. Error bars represent standard error on measured melt fraction. Source: Miller et al. (2014).*

When an interconnected melt network forms, the permeability of the partially molten rock can be quantified using a power-law relationship (e.g., McKenzie 1984; von Bargen and Waff 1986; Wark and Watson 1998; Connolly et al., 2009; Miller et al., 2014, 2015):

$$k = \frac{\phi^n d^2}{C}$$

where k is the permeability, ϕ is the melt fraction, n is the power law exponent, d is the grain size, and C is the geometric factor. The melt fraction is the volume fraction of melt in the partially molten rock, a term used interchangeably with porosity in this context. Higher melt fraction, i.e., higher porosity, corresponds to higher permeability. The power law exponent ranges in value and depends on the geometry of melt pockets. In an isotropic and homogeneous system, the values can be n=2 to n=3 and will have different geometric characteristics of melt pockets. When the geometry of the melt pockets are as thin cracks, a cubic law of n=3 applies (e.g., Snow, 1965). When the melt pockets are as tubes, theoretical, numerical and experimental studies show that n=2 (e.g., McKenzie 1984; von Bargen and Waff 1986; Zhu and Hirth, 2003). Experimental measurements of porous aggregates, including both rock analogs and the actual partially molten rocks, show that $2<n<3$ (e.g., Wark and Watson, 1998; Connolly et al., 2009; Miller et al., 2014, 2015). Such exponent values can be explained by the heterogeneity in real rocks (e.g., Zhu and Hirth 2003).

The permeability of partially molten rocks is sensitive to grain scale melt geometry. In sheared partially molten rocks, the applied stress alters the melt geometry and thus the permeability is expected to be different from the isotropic case described above. Experimental studies aimed at quantifying the permeability of sheared partially molten rocks are scarce (e.g., Zhu et al., 2017; Bader et al., 2019).

In this study, I will quantify the 3D melt geometry and permeability of an experimental charge and investigate the effect of shear strain on transport properties of sheared partially molten rocks. The 3D image was obtained using the X-ray synchrotron microtomogrpahy (SXμT). I performed image analyses to obtain the 3D melt distribution. I will then form the digital rock using the 3D melt distribution and calculate the permeability.

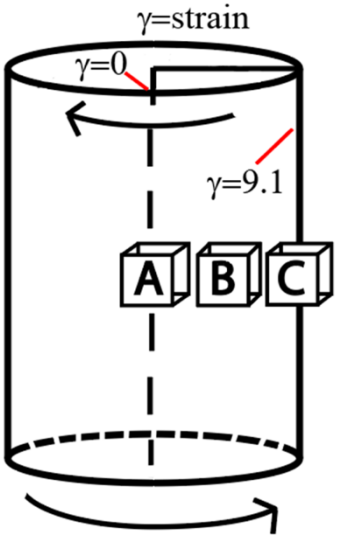

Fig. 4: *Relationship between Schematic of sample CQ0609A. The arrows indicate the torsion applied to the sample. Gamma (γ) represents the strain. At the center of the sample, the strain is zero. The very end of the sample the max*

3. Hypothesis

The permeability of the sheared partially molten sample has not been systematically quantified. The hypothesis to be tested is: at higher shear strain, melt will segregate into melt-rich and melt-poor regions and at low shear strain, melt distribution is more homogeneous. The permeability of melt-rich bands formed at high strain will be different from the melt-poor regions and will change as a function of strain. The stress-driven melt bands will be anisotropic in melt geometry and permeability. To test these hypotheses, I plan to calculate the permeability of a sheared partially molten experimental charge, CQ0609A, at low and high strains respectively and compare the results (Fig. 4).

4. Methods

4.1 Sample Preparation

The experimental rock sample was fabricated from fine-grained powder mixture of 90% olivine, representing the solid, from San Carlos, AZ, and 10% mid-ocean ridge basalt (MORB), representing melt, from the Mid-Atlantic Ridge (Qi et al., 2013). The mixture was cold pressed into nickel capsules in a uniaxial fashion at 100 MPa. The sample was then hydrostatically hot-pressed in a gas-medium apparatus at a temperature of 1473 K and pressure of 300 MPa for 3 hours. After hot-pressing, the samples were cut into thin cylinders and placed in silver capsules and enclosed in an iron jacket for deformation. The sample was deformed in a gas-medium apparatus fitted with a torsion actuator at 1,473 K and 300 MPa. The sample was torqued until the maximum strain of γ_{max} = 9.1 was achieved (Qi et al., 2018). Once maximum strain was achieved, the sample was cooled rapidly to 1,300 K under torque to preserve deformation-produced microstructure and then cooled to room temperature with no applied torque. This process developed stress-induced melt distributions in the sample.

4.2 Synchrotron X-ray Microtomography

Scans of the sample were obtained using synchrotron X-ray microtomogrpahy with the electron absorption microtomography imaging technique (Fig. 5) at a resolution of 0.16 micron per voxel. Scans were taken by rotating the sample 180° (Fig. 5) from γ_{min} = 0 to γ_{max} = 9.1 to create a series of image slices and digital volumetric representation of the sample. Each image slice is a greyscale image, where the pixels indicate the material density representing the differentiation between the melt and solid phases. The phase data are used to create a 3D microstructure digital image (Miller et al., 2014).

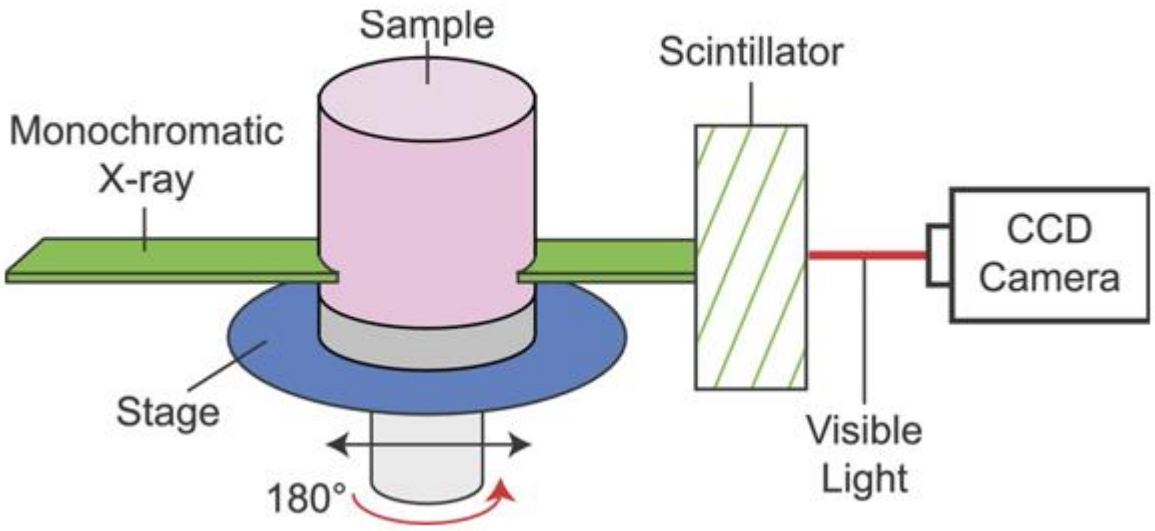

Fig. 5: *Diagram of imaging process. The sample has the monochromatic X-ray (green) transmit through the sample and onto a scintillator (dashed-green) that converts the signal to visible light (red) and is recorded by the CCD camera. The sample is rotated 180° during a microtomography experiment to create a series of cross-sectional data. Data that are used to create the 3D digital image. Source: Miller et al. (2014).*

4.3 Melt fraction

Qi et al. (2013) determined the melt fraction of the experiment CQ0609A using 2D micrographs. The 2D images were first processed using a Gaussian filter in MATLAB to reduce noise. A binary image was then created and melt fractions were calculated (area of melt/total area) (Fig. 6). The average melt fraction was found to be 0.055, with a maximum of 0.074 ± 0.017 and a minimum of 0.050 ± 0.005. (Qi et al., 2013).

4.4 Image processing and noise reduction

To analyze the digitized images, a series of filters were applied to binarize the 3D images using Avizo®, a ThermoFisher Scientific software package. Various filters were applied to preserve the image and maintain the melt fraction. Within the images, there is background noise and artifacts with a higher greyscale value that gets measured as melt when thresholding the image (Fig. 6). Thresholding distinguishes the melt from the solid phase and allows the melt and solid phases to be distinct. The pixels are assigned a value of either 0 for solid (black) or 1 for melt (blue). These two phases have different densities, which allows the greyscale values to be different. Within the solid phase, vast amounts of noise and artifacts are present. Therefore, to accurately measure melt and calculate permeability, it is necessary to filter out the noise and artifacts to threshold the image into a 2-pixel image.

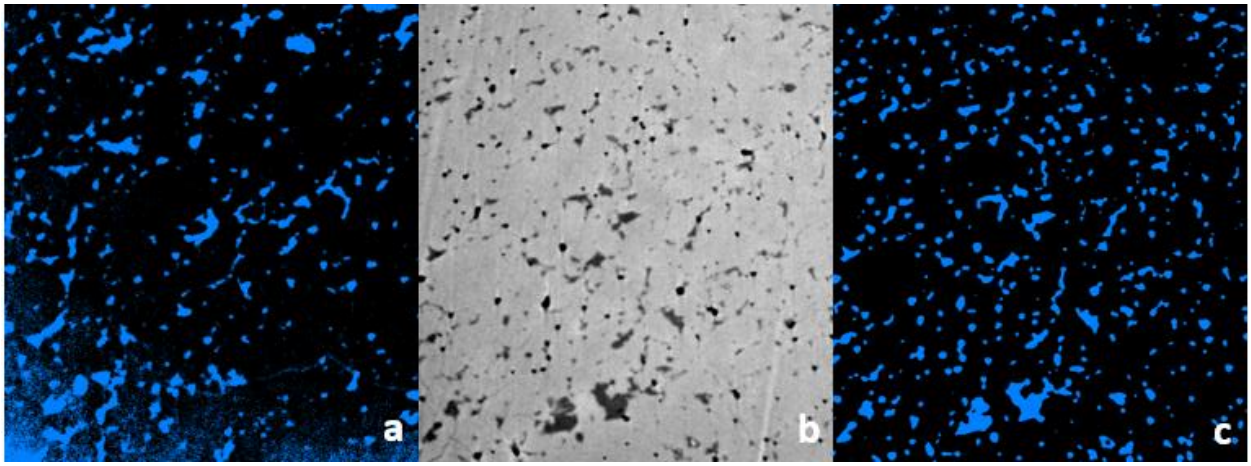

Fig. 6: *Zoomed in region of the γ_{max} image scaled at $2798\ \mu m\ x\ 2798\ \mu m$ to illustrate the effects the filters have on the image. Image b is the original image. Image a does not have a filter applied, while image c has had a series of filters applied. Image a has vast amounts of noise being measured as melt, while negating areas with melt and is not comparable to image b. Image a has a melt fraction of 0.17, significantly higher than range. Image c closely resembles image b and is not detecting noise from the image. Indicating the filters are appropriate and measures with a melt fraction of 0.073.*

To preserve the image while separating melt from the solid, filters were applied. A range of filters were tested such as edge preserving smoothing, shading correction, Gaussian, and other filters accessible in Avizo. To find the best filters to apply to the image, a small subvolume was selected to test various filters because the filters apply faster in a smaller region. A single filter can often take up to two hours to apply with a larger subvolume. Therefore, the smaller subvolume is ideal for discovering the sequence of filters required to filter out the noise and

artifacts, while being within the melt fraction range. Once the sequence of filters has been identified, a slightly larger subvolume is selected. At new or larger subvolumes, the filters sequence is applied. If melt fraction is still within range, another larger subvolume is selected and the procedure is repeated until the filters are applied to the entire image.

Each image, the high and low strain, have a different set of filter series applied. The individual filters used were background detection correction, shading correction, normalize greyscale and anisotropic diffusion. Each filter affects the image differently and has a purpose. Background detection correction and shading correction are greyscale transformation filters. These filters correct the background image greyscale to be more uniform, while considering individual pixel values. The filter normalize greyscale, and performs a linear scaling of the grey level values. This filter also enhances the overall contrast in the image. To smooth the image and reduce noise, the filter anisotropic diffusion was used. Lastly, interactive threshold was applied, and this creates the 2-pixel image of blue and black. This filter was applied after each filter to detect melt and see if noise and artifacts were being perceived as melt. There is uncertainty defining the border between melt and solid within the voxels.

A) Minimum Strain (γ_{min} = 0)

The minimum strain value of 0 had various artifacts and noise (Fig 7). Artifacts observed are rings located in the center, shadows on the corners, and "rain", that are small streaks. However, due to the extreme shadows along the edges of the image, a subvolume of 1198 μm x 1376 μm x 2033 μm was selected from the whole image of 2048 μm x 2048 μm x 2033 μm to accurately represent and measure melt. The filters could not filter the shadows without distorting the image significantly.

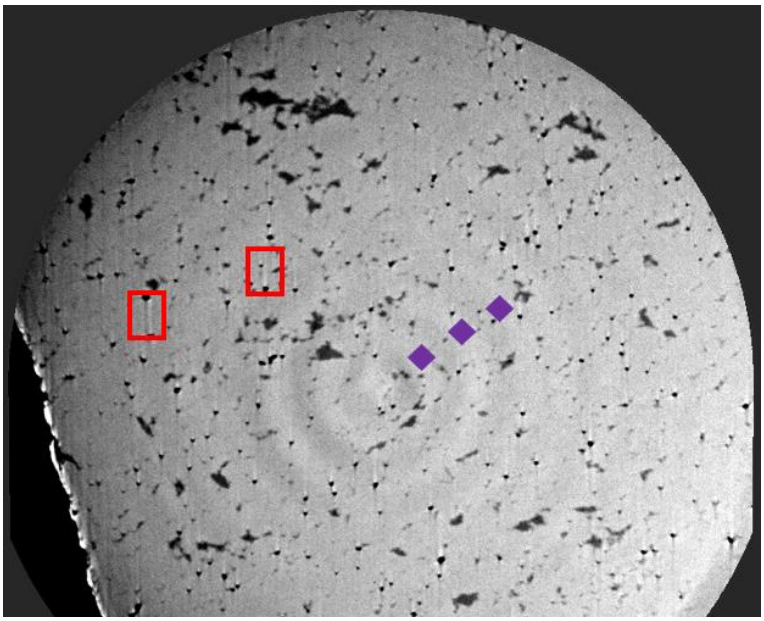

Fig. 7: *Image of the minimum strain values artifacts and noise. Red rectangles represent examples of the "rain" that is present throughout the image. The purple diamonds are locations of the rings. Image scaled at* $2048\ \mu m\ x\ 2048\ \mu m$.

The image had a sequence of filters used (Fig.8). Background detection correction was used to generate a uniform background greyscale, but noise and artifacts were still detected. Also, the greyscale value reduced the melt greyscale and developed small holes within the melt regions. To correct for noise, the filter normalize greyscale, was used. This enhanced the contrast, blended the background noise and reduced the rain. However, the background still had noise being detected and holes still seen. The shading correction filter was used to counter this. This reduced the noise that was being detected, but it did not smooth the image. To smooth the image and

correct greyscale melt holes, anisotropic diffusion was used. Lastly, interactive threshold was used to distinguish melt. A melt fraction of 0.078 ± 0.014 was computed using the volume fraction tool.

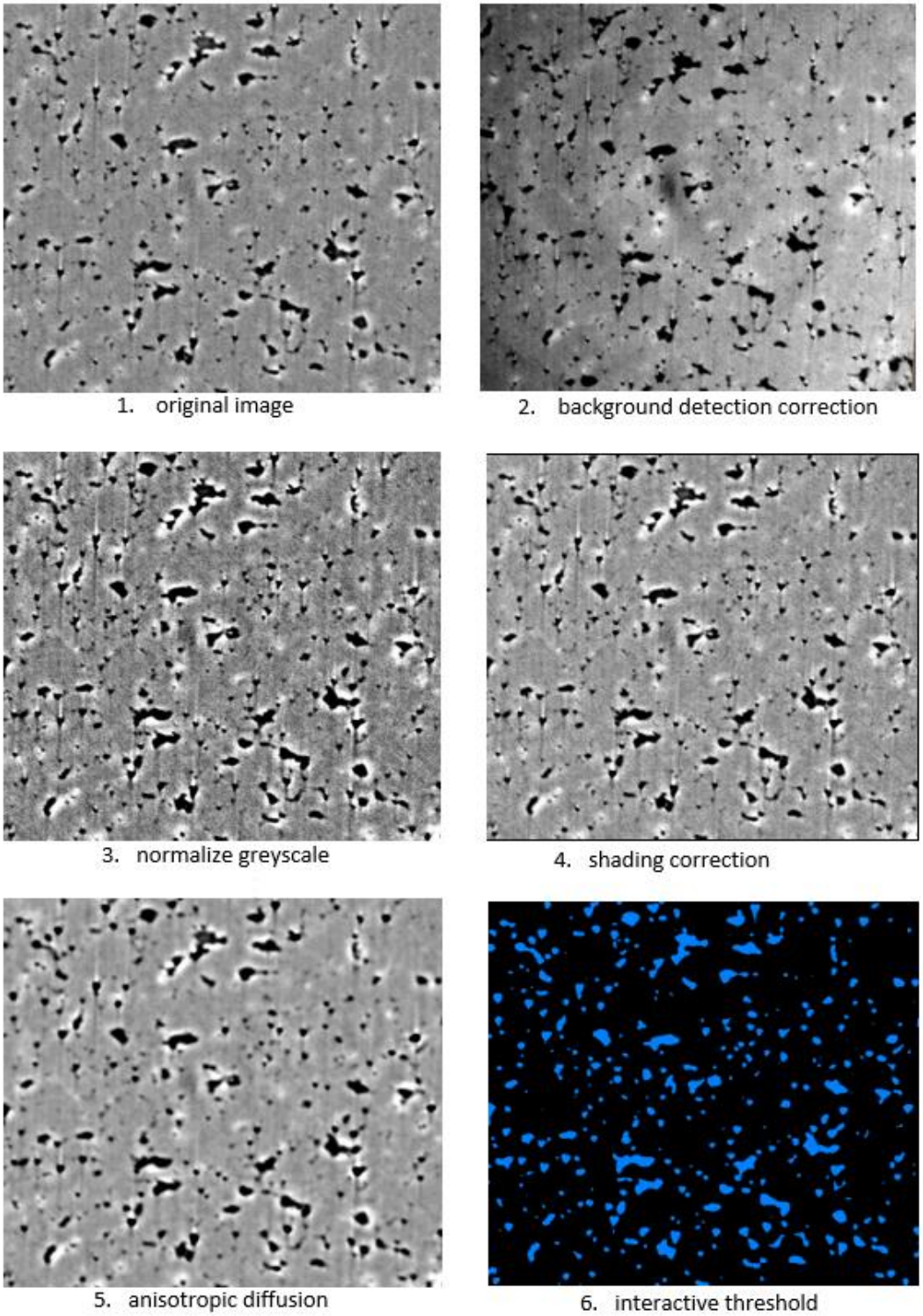

Fig. 8: *Images of the range of filters applied to γmin. Scale of images is 550 μm x 550 μm.*

B) Maximum Strain (γ_{max} = 9.1)

The maximum strain value of 9.1 has a region that appears “damaged”. However, this region is located at the end of the sample and the mixture created this distortion (Fig. 9) (Qi et al., 2013). The artifacts observed are cracks that were formed during cooling and decompression (Qi et al., 2013) along with background noise.

The entire image was applied with a sequence of filters. First, the background detection correction was used. Noise and cracks were still being detected. To correct this, normalize greyscale filter reduces the noise and tones the crack pixel value and was applied. Then, to smooth the image, anisotropic diffusion was used. This smoothed the background noise and cracks. Finally, the interactive threshold was applied and a melt fraction of 0.073 was computed. The illustration of the filters can be seen in Fig. 10. It is evident that in the deformed part of the scan a few cracks were still being detected. These cracks being detected were manually removed using the segmentation tool (Fig. 9). They were removed because this artifact is clearly not melt, but an artifact being detected as melt.

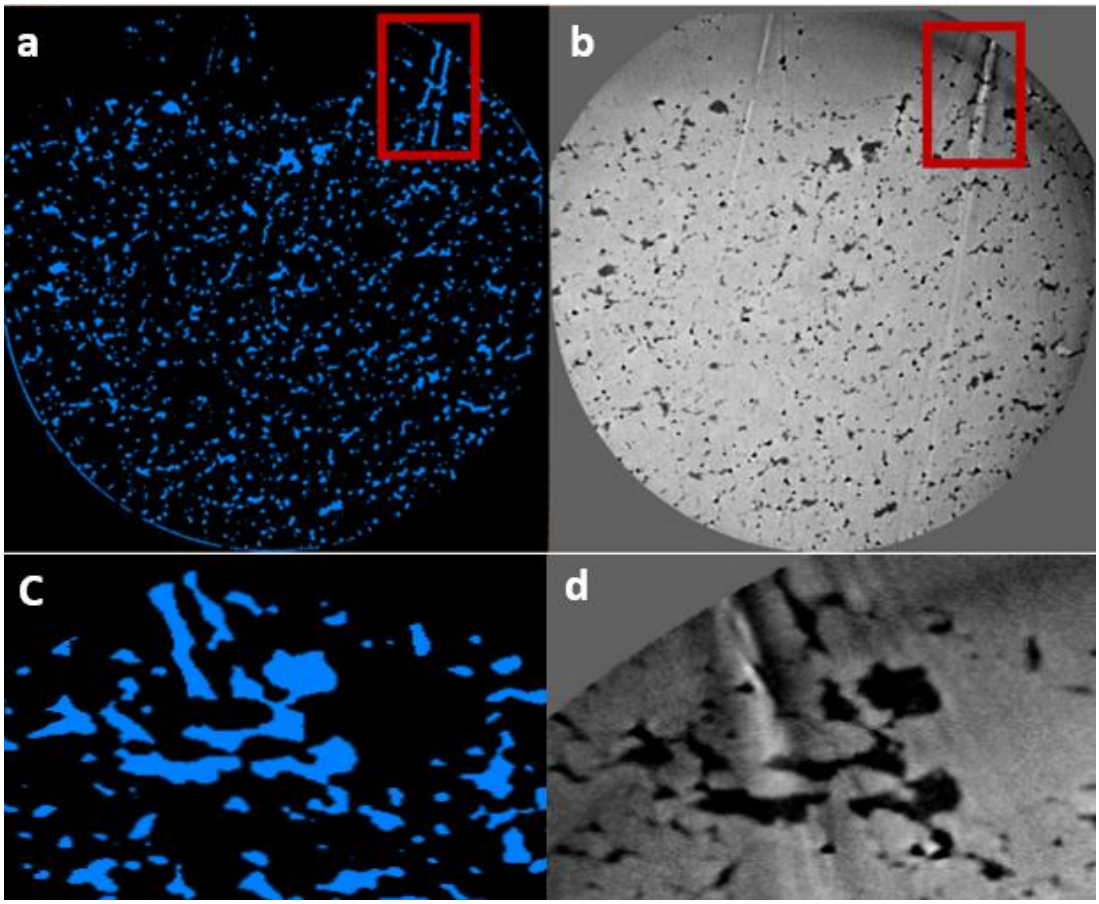

Fig. 9: Image of the entire scan where filters were applied. Image a has been filtered and is seen with the interactive threshold filter. Image b is original scan with no filters applied. Red box illustrates the crack that has not been filtered out. Top part of the scan is b that appears bald, is the distorted region. Images a and b scaled at $2798\ \mu m\ x\ 2798\ \mu m$. Image c and d are zoomed in regions. Image c is the manual removal of the cracks that were detected as melt. Image d is the non-thresholded image.

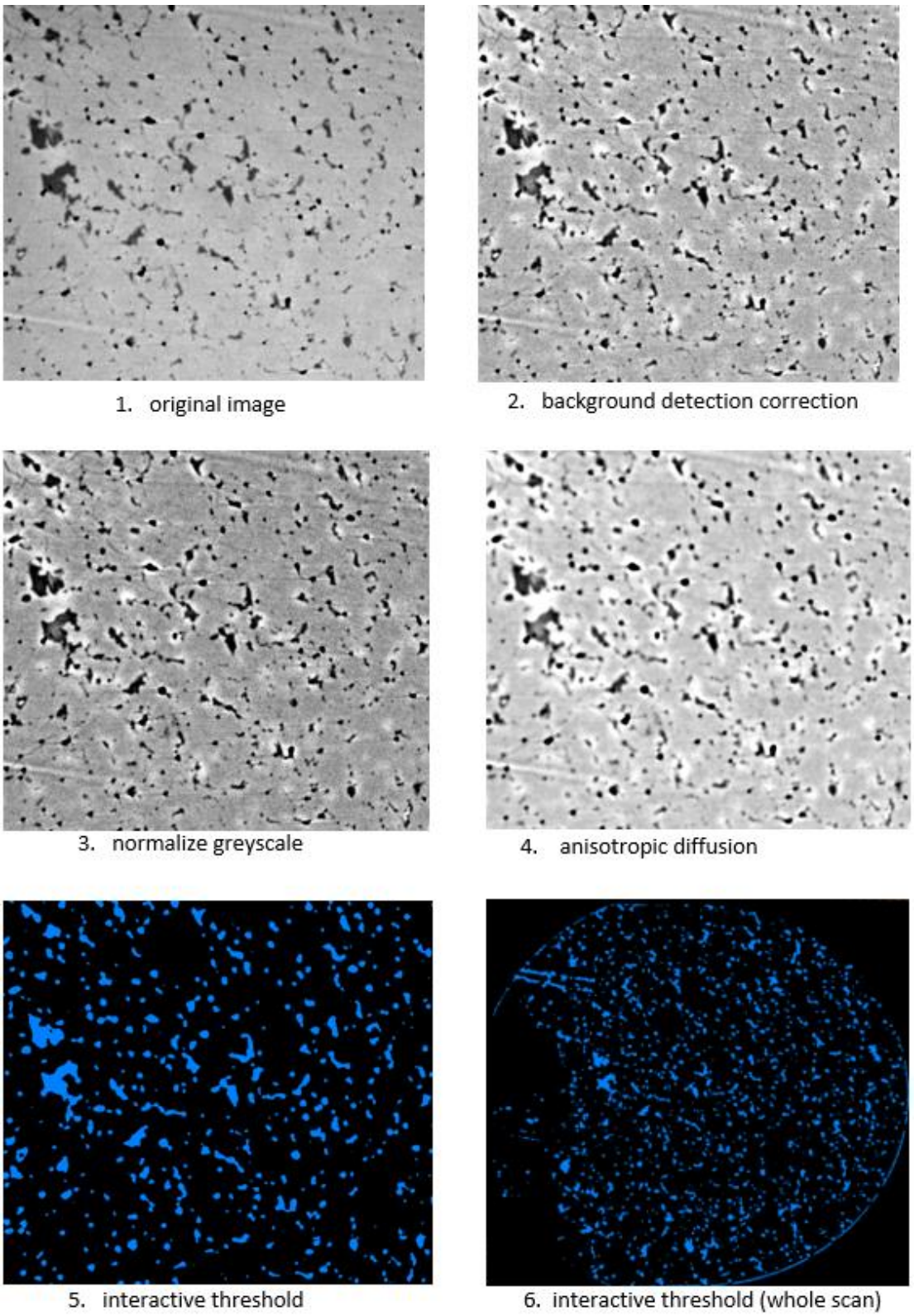

Fig. 10: *Images of the range of filters applied to γ_{max}. Scale of 2798μmx2798μm for the whole scan (panel 6), other images zoomed in from whole scan.*

4.4 Connectivity, Melt Fractions, and Permeability Calculations

Once the images were filtered, the permeability can be tested. This is tested by first measuring the connectivity. To test for the connectivity, the axis connectivity module is applied. This module measures in the X, Y, and Z direction and informs what direction the melt band is located from the threshold image (Fig. 11).

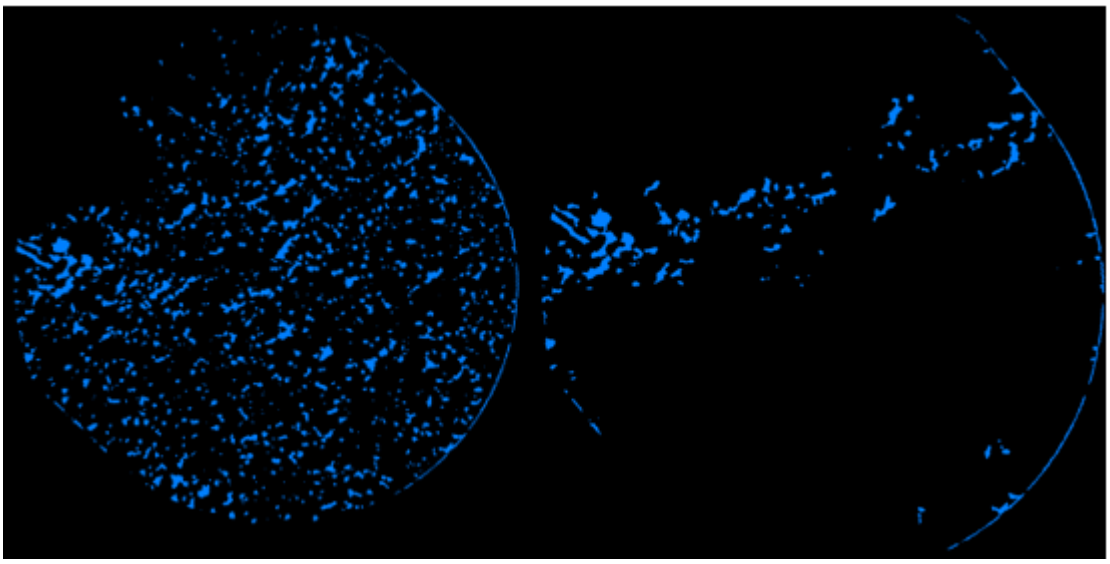

Fig 11: *Left image is entire threshold image for γ_{max} , scaled at 2798μmx2798μm. Right image is the melt band in the Z direction, when the axis connectivity modules was applied.*

Once connectivity is found. The selection of various sized subvolumes was made throughout the region of the melt band to observe melt-rich and melt-poor regions within the band. Then, in each subvolume, connectivity was tested in the X (across-band), Y (along-band) and Z (along-band) directions. Once the direction or directions were established, the permeability test could be started. To measure permeability, the module Absolute Permeability Experiment Simulation (APES) was used. This module computes the permeability in one direction for the selected subvolume. A one-pixel impermeable surface is applied to four faces of the subvolume, resulting in two open parallel planes. To eliminate bias in large and small pore spaces on the edges of the subvolume, 10 pixels are added to each side of the subvolume and manually selected to run two convergence criterions at 10^{-6} and 10^{-8}. Two values are selected to measure the convergence of the permeability at a higher value.

To determine if the melt is heterogenous or homogenous, melt fractions were taken throughout the sample. This was done by dividing the sample image into three large regions, then measuring the melt fraction with 32 sized 200 µm x 200 µm x 200 µm subvolumes in each region, totaling in 96 melt fraction regions. Data were compiled into a histogram to establish if melt is heterogenous or homogenous.

A) Minimum Strain (γ_{min} = 0)

When the axis connectivity was applied, there was no connectivity in any direction. To ensure there was no connectivity, subvolumes of 40 µm x 40 µm x 40 µm, 80 µm x 80 µm x 80 µm, 1300 µm x 1300 µm x 1300 µm, and 200 µm x 200 µm x 200 µm were selected. The axis connectivity tool was applied to the various subvolume sizes. This was done until each subvolume size covered the entire image. The entire region was then selected, and the axis-connectivity tool was applied. There was also no connectivity found (Fig.12). Therefore, the APES modulus was not used. Also, with no connectivity found, the melt fraction was measured throughout the sample by dividing the sample into three regions (Fig. 13).

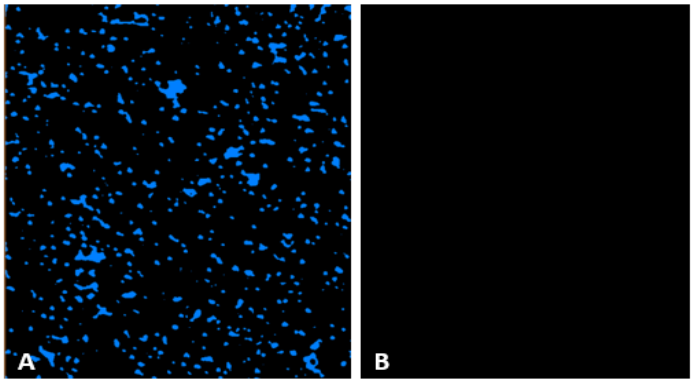

Fig. 12: *Connectivity results for γ_{min}=0. A is scan before axis-connectivity module applied. B is the result of the module being applied. It is blank because no connectivity was found at low strain.*

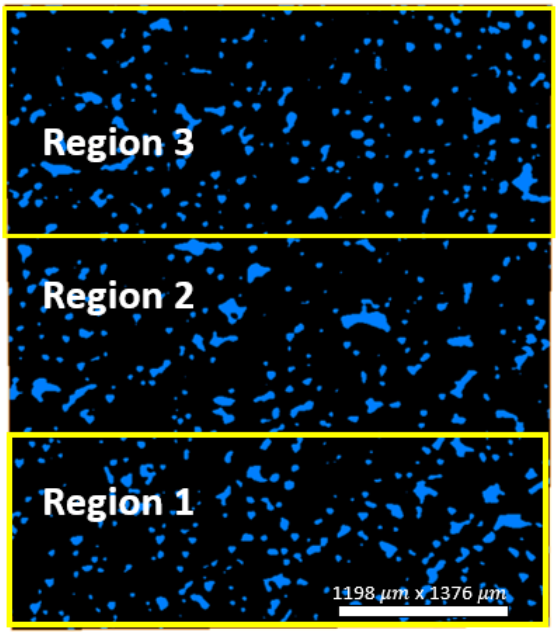

Fig. 13: *The three divided regions in the γ_{min}=0.*

B) Maximum Strain (γ_{max} = 9.1)

Connectivity was found within melt bands formed at γ_{max} = 9.1 (Fig. 12). Because the melt connectivity and geometry are anisotropic in the melt-rich bands, it is important to investigate the permeability anisotropy within the melt-rich bands. Stress-induced melt bands are largely planar features, 3 principal permeability components, i.e., one across-band and two along-band component will be calculated.

In the default coordinates used by Avizo, the Z-axis is along the axial direction of the scanned sample reconstructed from the microtomographic datasets. The melt bands are found at ~43° with respect to the Z axis and 4° around the X axis (Fig. 14 left). To obtain the permeability components along and across the melt bands following the default Avizo coordinates, we first rotate the images so that the Z and Y directions are along the bands and X direction across the band (Figure 14, right).

The image was then divided into three regions to calculate the melt fractions (Fig. 15a). The regions were divided into melt-poor regions, where the melt-band is not located, and melt-rich region where the melt band resides.

Then, within the melt-band, three sites were selected (Fig. 15b) and the permeability was calculated using 4 different sized subvolumes of $250\mu m^3$, $200\mu m^3$, $150\mu m^3$, and $100\mu m^3$ (15b). This was used to represent a regions permeability trend with different subvolume sizes. That provides insight on which subvolume size to use when running the permeability calculations. If the subvolume size is too small, the region might be a melt pocket and the melt-band network is not being represented. If the subvolume is too large, the region may be calculating too much of the un-banded regions which is also not a true representation of the banded network.

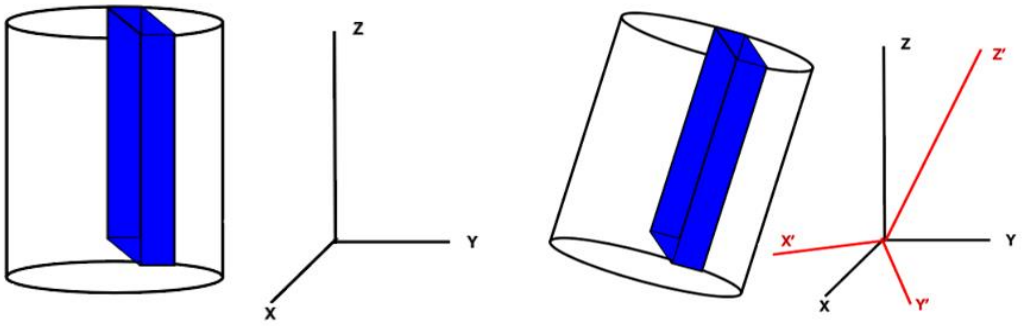

Fig. 14: *Images of the melt band from γmax. Image a illustrates how the band is not align with Avizo's coordinate system. While, image b was rotated 43° around the Z axis and 4° around the X axis. Aligning the Avizo's coordinate system to the image. The X' axis is against band, while Y' and Z' axis is along band. Figure not to scale. Note: X (across-band), Y (along-band), Z (along-band).*

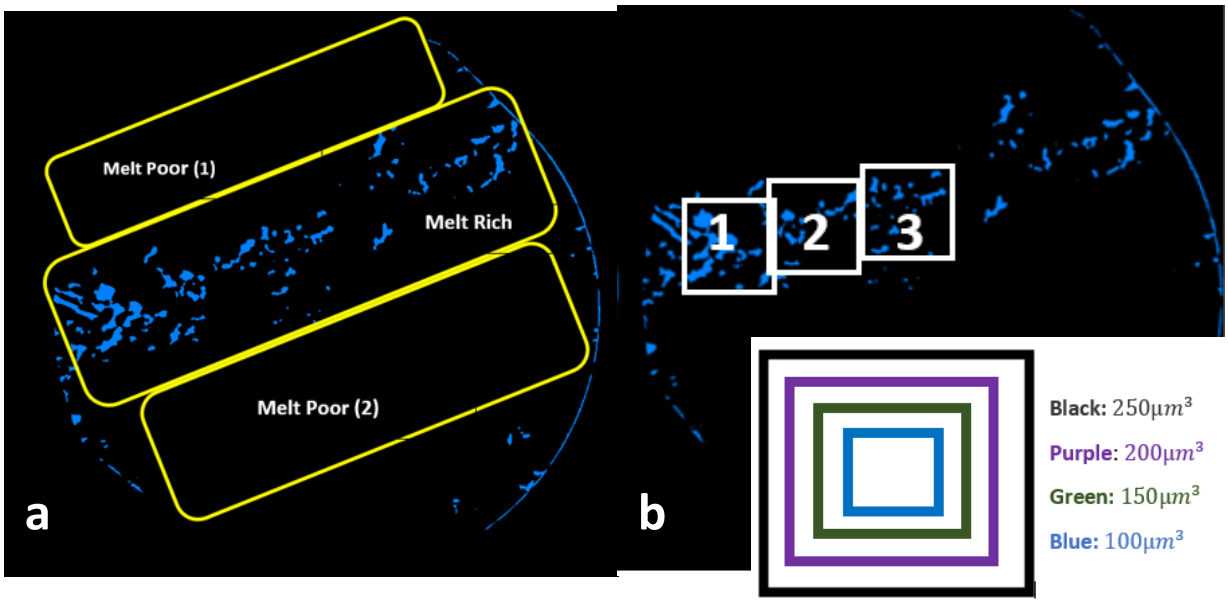

Fig. 15: a) *The γmax sample divided into three sections. Melt poor regions is where the melt band is not located. Melt rich region is where the melt band is located. b) is the 3 sites that were chosen on the melt band. The pop out figure is illustrating how the subvolumes changed in size.*

5. Results

A) Minimum Strain (γ_{min} = 0)

The minimum strain image was analyzed for permeability. The permeability was tested by measuring the connectivity using Avizo®. Various sized subvolumes were selected from the binarized image to check for connectivity in the image. At the minimum strain, no connectivity was found indicating there is no permeability when the strain is zero. Indicating that at zero strain, the melt distribution is homogenous. This was shown by having the scan divided into three regions (Fig. 13) and measuring a total of 96 melt fractions. The data (Fig. 16) shows that the melt fraction averages in Region 1, Region 2 and Region 3 being 0.085, 0.079, and 0.084, with standard deviations of 0.013, 0.008, and 0.01 respectfully.

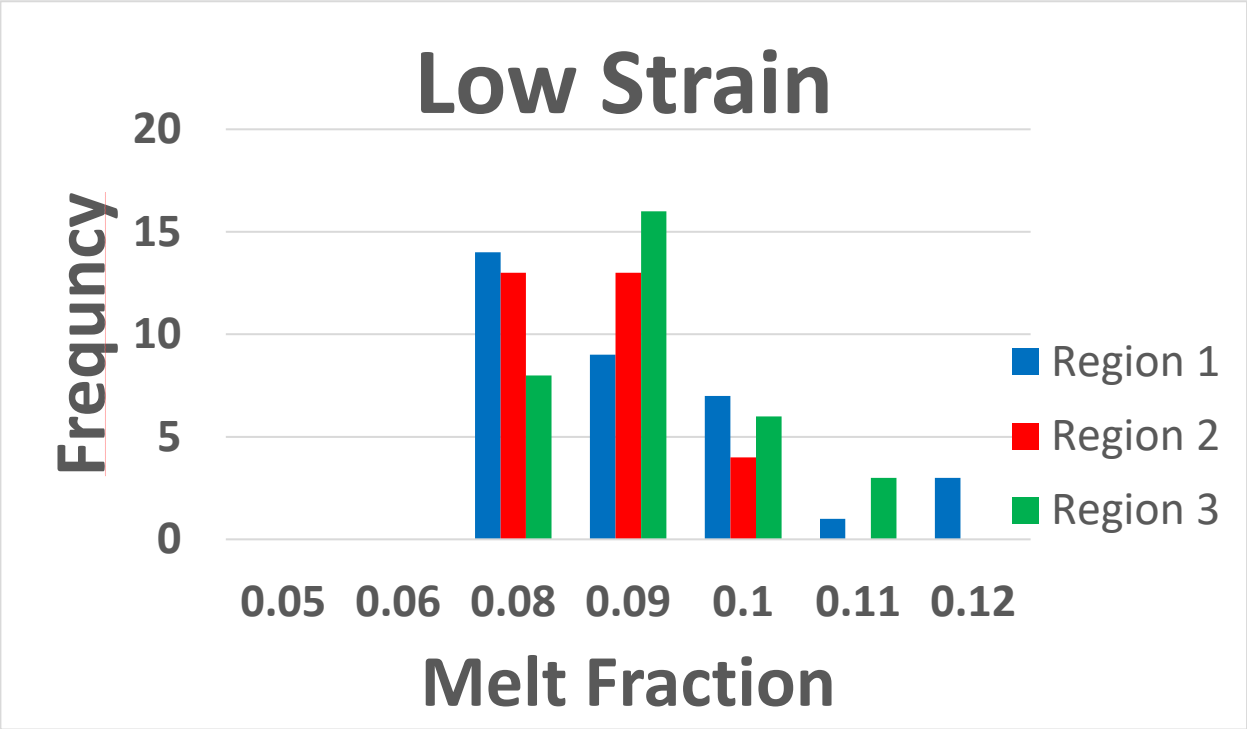

Fig. 16: *Melt fraction distribution of γ_{min}. Averages are 0.085 (Region 1), 0.079 (Region 2), and 0.084 (Region 3).*

High Strain

The maximum strain was analyzed for permeability and a melt band was established. With the melt band established, the sample was divided into three regions (Fig. 15) and the melt fractions were calculated. In Fig. 17, the histogram of the melt fractions and the region is distributed. The Melt-rich, Melt-poor (1), and Melt-poor (2) have melt fraction averages of 0.134, 0.033 and 0.092, with standard deviations of 0.027, 0.059 and 0.0086 respectfully. The melt band has a significantly higher melt fraction compared to the melt poor region.

Since the melt-band region does have a higher melt permeability, the 3D melt network shows the melt connected channels in the stacked image series. This was found by using the melt band and creating a 3D image of the scans (Fig. 18). The red is the melt that is connected, and the connected melt region corresponds to where the melt band is located. By using a large subvolume that has melt outside of the band, it is seen that outside of the melt band, the melt is not connected (Fig. 19). In Fig. 19 the red is the connected melt while the grey is non-connected melt or loose melt pockets. Using this plot, three sites were selected to measure the permeability (Fig. 15b).

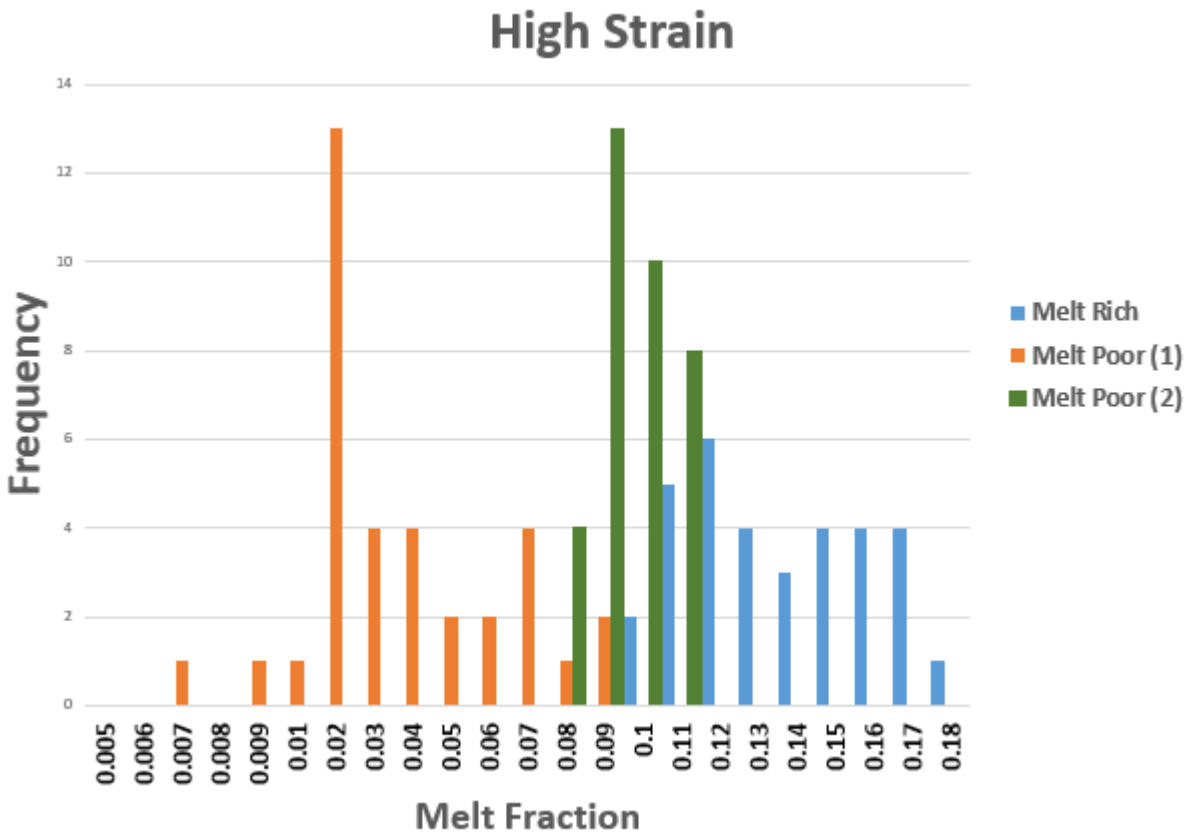

Fig. 17: *Histogram of ymax with melt fraction averages of 0.134 (Melt Rich), 0.033 (Melt Poor 1), and 0.092 (Melt Poor 2).*

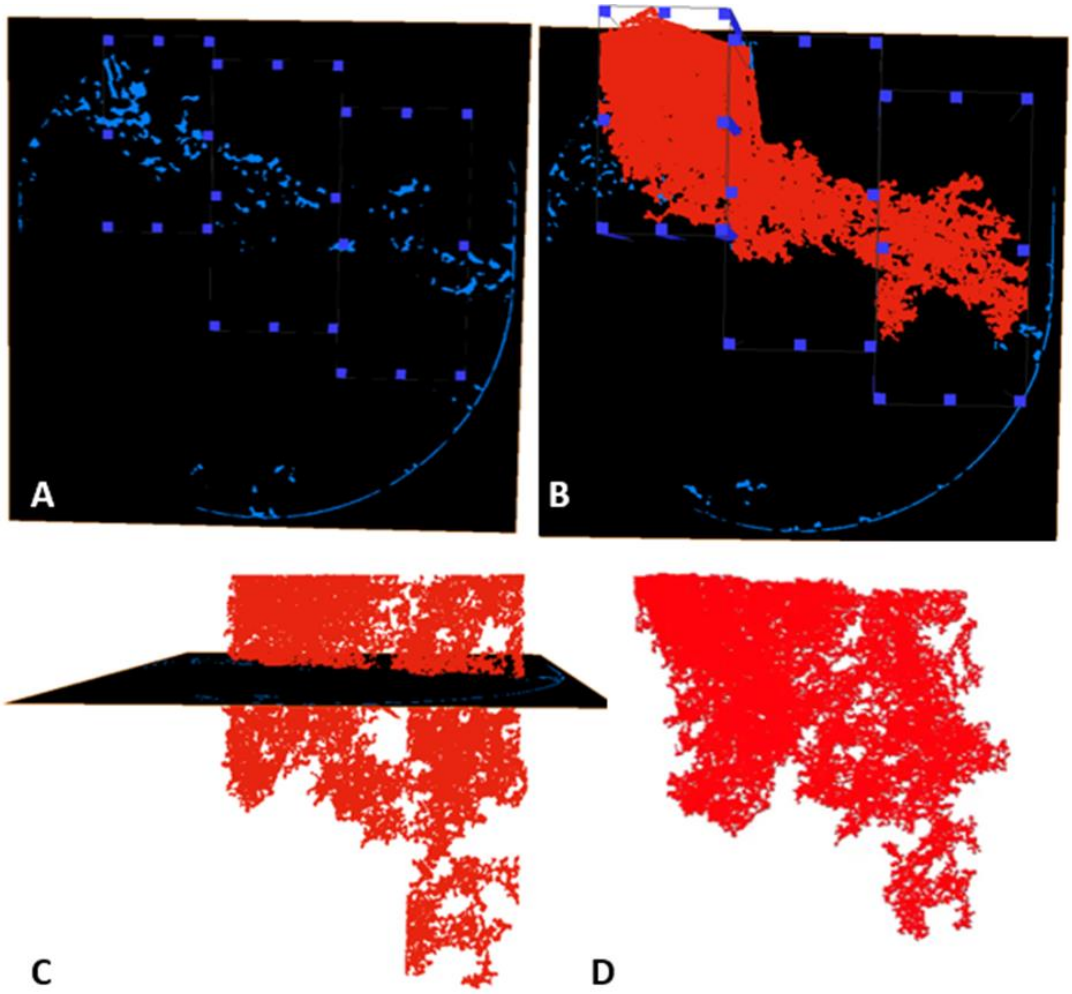

Fig. 18: *Images showing where melt is connected (red). A is showing the region where the large subvolumes were taken. B is demonstrating the connected melt on the scan. C is showing the 3D connected melt (red) in respect to the scan. These scans are stacked creating the 3D image. D is the whole melt connected network within the scan.*

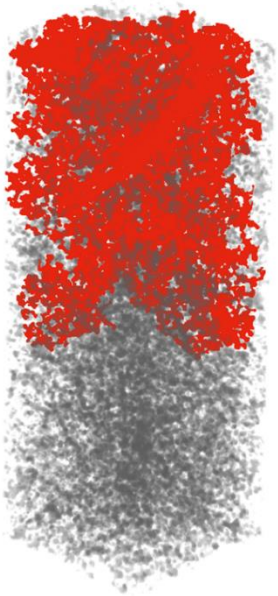

Fig. 19: *Portion of the melt connected network. Red is where the melt is connected, and grey is non-connected melt or loose melt.*

The three sites were selected along the melt-rich band. For each site, a subvolume sized $250\mu m^3$, $200\mu m^3$, $150\mu m^3$, and $100\mu m^3$ was calculated (Table 1). At each site and subvolume, the melt fraction was calculated, and the permeability was calculated in the X (across-band), Y (along-band) and Z (along-band). The data was then plotted as Permeability vs Subvolume (Fig. 20) and Melt Fraction vs Subvolume (Fig.21). These two plots are used to determine the subvolume size that best represents the permeability and melt fraction. The $250\mu m^3$ and $200\mu m^3$ subvolume was chosen, and they were graphed (Fig. 22 and Fig. 23) as Permeability vs. Melt Fraction. The slope was found between the data points in each direction for each subvolume. Also, the

slope was found using Miller et al., 2014 and plotted to show the difference in slope (Fig. 22 and Fig. 23).

Site #	Melt Fraction (Φ)	Subvolume μm^3	Permeability (k) m^2 X (across-band)	Permeability (k) m^2 Y (along band)	Permeability (k) m^2 Z (along band)
Site 1	0.188286	250	9.12E-16	6.59E-15	3.05E-15
	0.196439	200	4.06E-15	5.01E-15	3.22E-15
	0.201404	150	3.82E-15	5.98E-15	3.29E-15
	0.240772	100	2.03E-15	4.92E-15	4.7E-15
Site 2	0.133568	250	9.8E-17	9.44E-16	1.69E-15
	0.157753	200	1.45E-15	1.04E-15	7.66E-16
	0.16334	150	5.08E-15	7.31E-15	1.64E-15
	0.214072	100	5.09E-15	7.32E-15	1.65E-15
Site 3	0.138116	250	3.19E-16	4.4E-16	8.05E-16
	0.146453	200	5.21E-16	8.37E-16	1.13E-15
	0.137613	150	7.87E-16	7.75E-16	1.69E-16
	0.172387	100	1.62E-15	1.37E-15	2.47E-15

Table 1: *Data for each site with respected melt fraction at each subvolume size and permeability calculations for the X (across-band, Y (along-band) and Z (along-band) directions.*

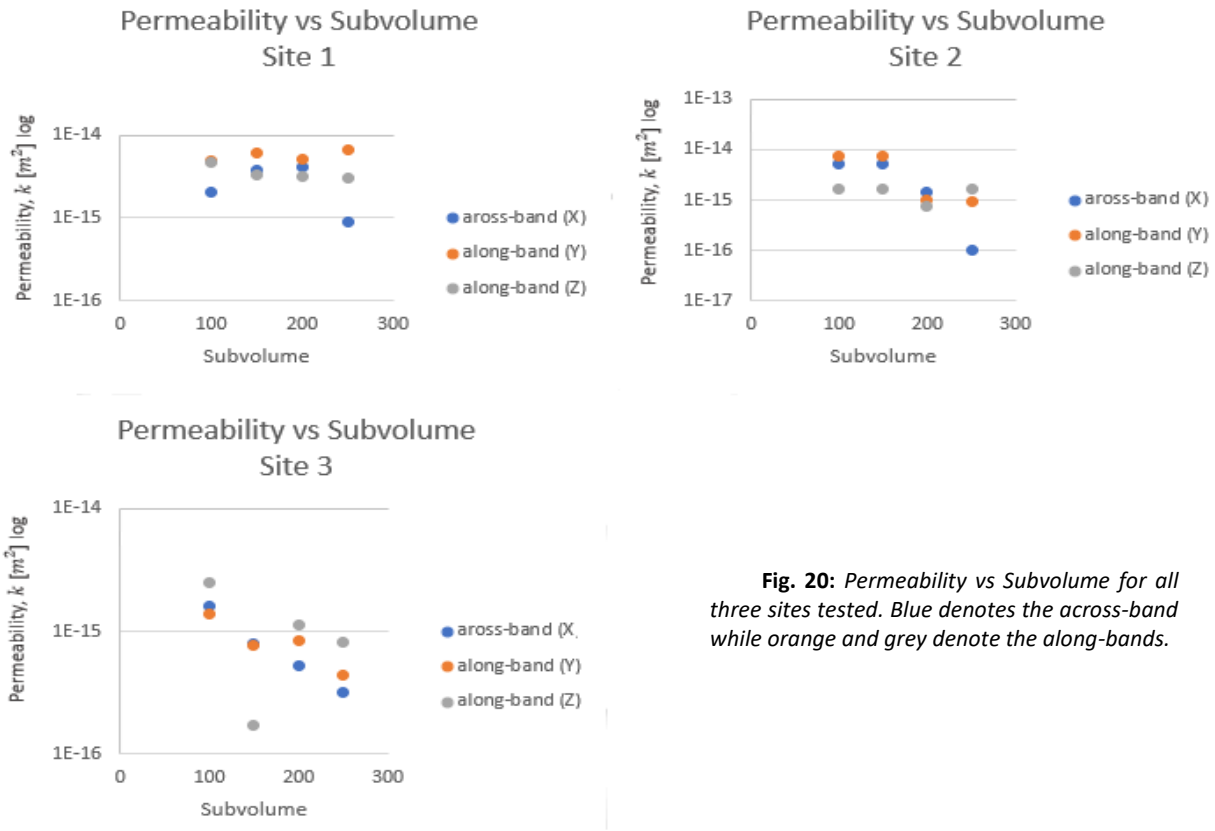

Fig. 20: *Permeability vs Subvolume for all three sites tested. Blue denotes the across-band while orange and grey denote the along-bands.*

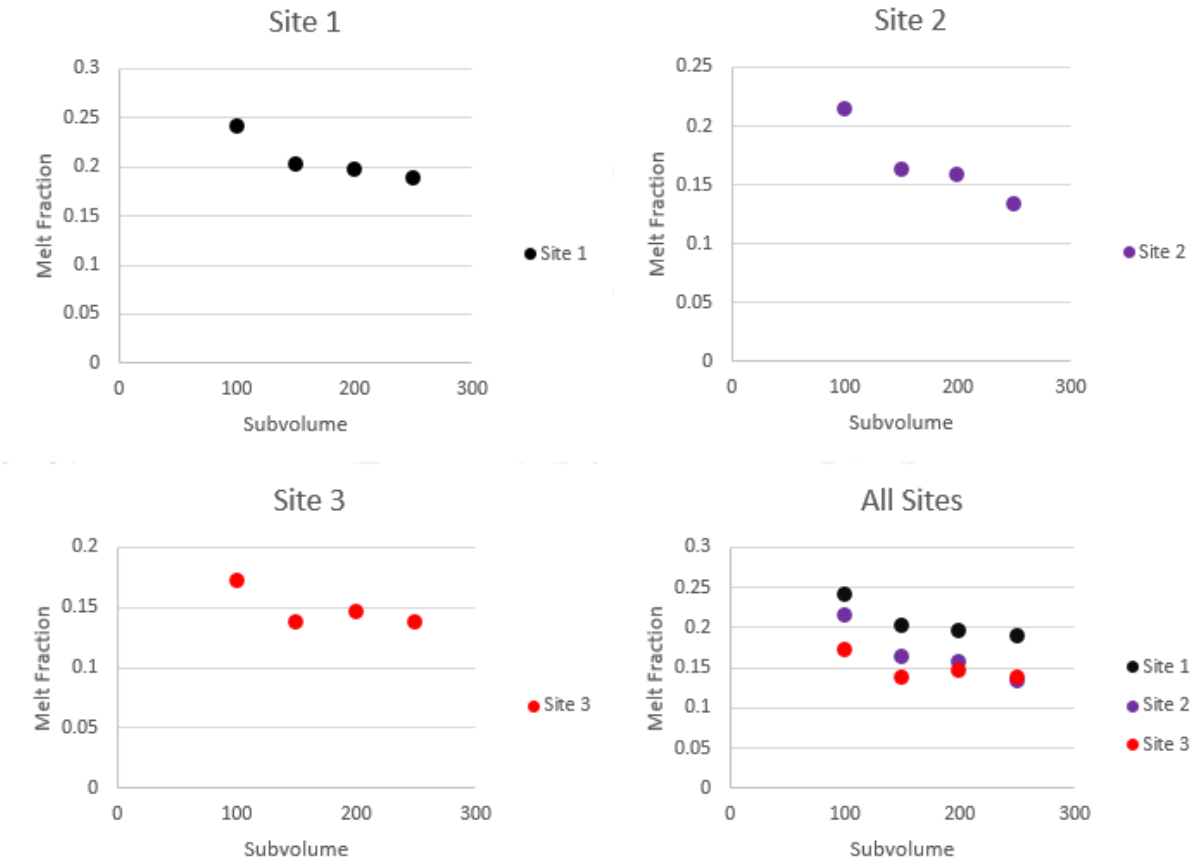

Fig. 21: *Melt Fraction vs Subvolume for each site. Black is site 1, purple is site 2, and red is site 3.*

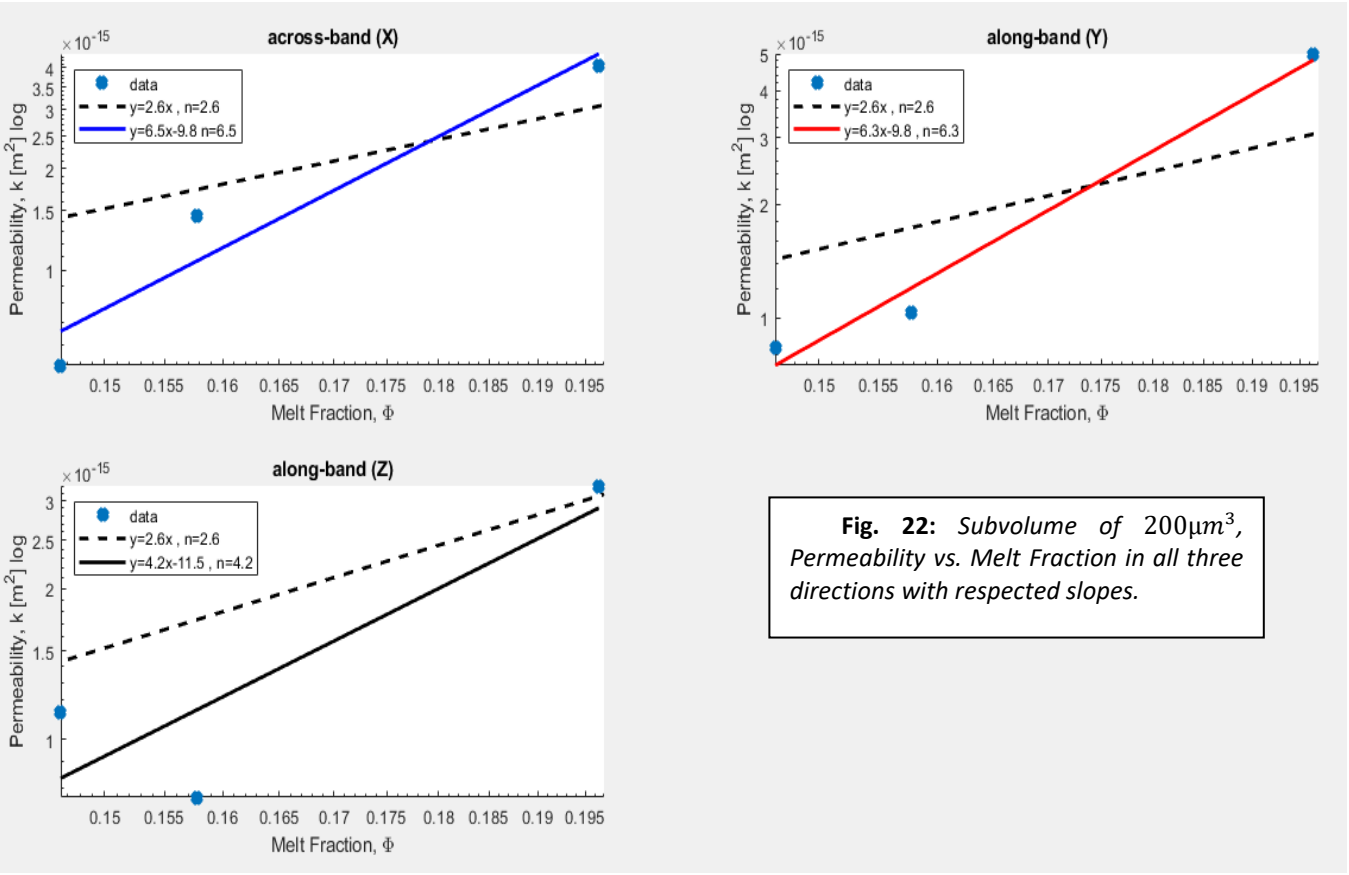

Fig. 22: *Subvolume of* $200\mu m^3$*, Permeability vs. Melt Fraction in all three directions with respected slopes.*

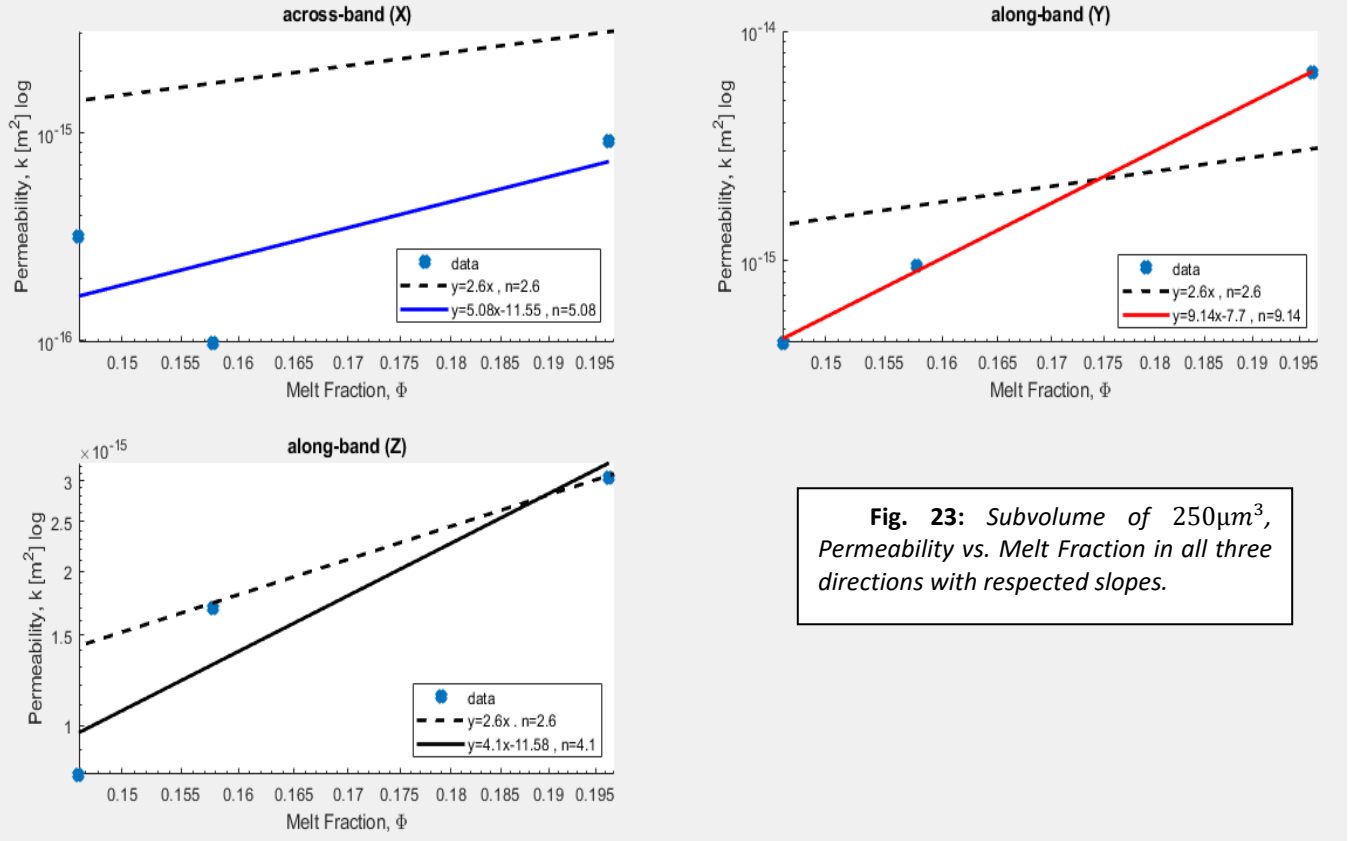

Fig. 23: *Subvolume of* $250\mu m^3$*, Permeability vs. Melt Fraction in all three directions with respected slopes.*

6. Discussion

The low strains averages of 0.085 ± 0.013, 0.079 ± 0.008, and 0.084 ± 0.01 with a total average melt fraction of 0.083 ± 0.032 and percent error of 38.6%. The absolute minimum is 0.06 and absolute maximum is 0.12. The significance was tested using One-Way ANOVA with a significance level of 0.05 and calculated a p-value = 0.028. Using a hypothesis that the melt distribution is heterogenous, and a null hypothesis that the melt distribution is not heterogeneous. The p-value of 0.028 is significant at $p < 0.05$ and we fail to reject the null hypothesis. In comparison the high strain averages of 0.134 ± 0.027, 0.033 ± 0.059 and 0.092 ± 0.009, have a total average melt fraction of 0.086 ± 0.027 , a percent error of 31.4%, and an absolute minimum of 0.007 and absolute maximum of 0.20 The significance was also tested using One-Way ANOVA at a significance level of 0.05 to calculate that the p-value < 0.00001. The p-value of <0.00001 is highly significant at $p < 0.05$ so we fail to reject the null hypothesis and accepting that the melt distribution is heterogenous.

Although the low strain is accepting that the melt distribution is heterogenous, the melt region may be more homogeneous then heterogenous. In Fig. 16, the melt fraction distribution is skewed right. The skewness shows that there are more lower melt fractions compared to higher melt fractions. However, region 3 does have a clear peak and having a unimodal distribution. However, this could be caused by the melt fraction being taken near the edge of the sample, which can cause higher melt fractions. Also, in Region 1 and 3, who have similar averages, there is an overall higher melt fraction compared to Region 2.

This could be from the randomness of selecting the subvolumes within each region. Also, the absolute minimum of 0.06 and absolute maximum of 0.12, has a spread of 0.06 and this lack in variation could result in why the data has no distinct pattern in each region, resulting in the skewness. In comparison, the high strain data in Fig. 17 has distinctive peaks and are unimodal within each region. The melt-poor regions have lower melt fractions compared to the melt-rich region. Each region has a peak that is significantly different then another region. The spread of the data is also larger, with the absolute minimum of 0.007 and absolute maximum of 0.20, that has a spread of 0.193. This high spread of the data could be the result from there being melt-depleted regions and melt-rich regions. These melt-depleted regions have lower melt fractions, and the melt-rich regions have higher melt fractions. This difference suggest that the melt is heterogenous. As oppose to the low strain where there is lower data spread, less variations of the data and has no melt-band. This suggest that the low strain may be more homogenous and less heterogenous. Therefore, based on the data and the statistical analysis the low strain is more homogenous, and less heterogenous, while the high strain is heterogeneous.

Since the high strain has connected melt, thus permeable, three sites were selected along the band (Fig 15b). Each site had subvolumes sized $250\mu m^3$, $200\mu m^3$, $150\mu m^3$, and $100\mu m^3$ calculate permeability in X (across-band), Y (along-band), and Z (along-band) (Table 1). The purpose of using various sized subvolumes is to find a subvolume that will best measure and represent the permeability calculations.

The data was plotted as a Permeability vs. Subvolume for each site (Fig. 20). This plot was used to decide which subvolume should be used to most accurately measure the permeability. The three graphs show that the $150\mu m^3$, and $100\mu m^3$ subvolumes have similar permeability

results. Except at Site 3 where the $150\mu m^3$ subvolume is significantly lower. This may be an outlier and be caused by the region that was being measured. The $250\mu m^3$, $200\mu m^3$ subvolumes were also similar with their melt fractions at all three sites. Then, the data was plotted as Melt Fraction vs. Subvolume (Fig. 21) for each site. This graph is to show how the subvolume size changes the melt fraction. Which, in all three graphs there is a decrease in the melt fraction as the subvolume size increases. It also indicates that at $250\mu m^3$, $200\mu m^3$, and $150\mu m^3$ the melt fraction gradually increases and then becomes significantly larger at $100\mu m^3$. This abrupt increase might be because at $100\mu m^3$ the subvolume is calculating too small of a region to measure the flow. Based on these graphs, the subvolumes $250\mu m^3$ and $200\mu m^3$ were chosen to be used to represent the melt fraction and permeability calculations. These subvolumes were both consistent with one another in all figures, which establishes them as the best representation.

The $200\mu m^3$ and $250\mu m^3$ subvolumes where then plotted as Permeability vs Melt Fraction in log scale. Fig. 22 represents the $200\mu m^3$ subvolume, and Fig. 23 represents the $250\mu m^3$ subvolume. In Fig. 22, the across-band (X) had a best-fit-line with a slope of y=6.5x - 9.8 with n=6.5, along-band (Y) had a slope of y=6.3x – 9.8 with n=6.3, and the along-band (Z) had a slope of y=4.2x - 11.5 with n=4.2. In Fig. 23 the across band (X) had a slope of y=5.08x – 11.55 with n=5.08, across-band (Y) had a slope of y=9.15x - 7.7 with n=9.15, and across-band (Z) had a slope of y=4.1x-11.58 with n=4.1. The slope for the dashed line in all plots is y=2.6x with n=2.6 (Miller et al., 2014). For all graphs in Fig. 22 and Fig. 23 the slope of the data points is higher than that found in Miller et al., 2014. Which was calculated in a sample that was undeformed versus the deformed sample, that was calculated in this study. So, in a deformed sample the slope and n value are higher then that of the undeformed sample. Although there is only three data points per subvolume and direction, there is indication that when you consider shear strain in a deformed sample, the melt fraction increases at a faster rate. In other words, with higher permeability calculations could mean faster melt movement.

However, more data points need to be calculated to determine the trend. Also, by repeating this process for a medium strain would provide more insight on the effects of shear strain on permeability.

7. Conclusion

In this study, the effects of shear strain on melt distribution and permeability was quantified. I applied various image analysis tools on the X-ray synchrotron microtomography images and created a 3D melt distribution to form a digital rock and conduct virtual flow through experiments to calculate their permeability. At low strain I found no connectivity, and the melt to be more homogenous and isotropic. At high strain I found melt connectivity, melt to be more heterogenous and anisotropic, and a higher slope an n value. This provides new constraints on channelized melt transport of partially molten regions beneath ocean ridges.

Acknowledgments

First and foremost, I would like to thank my advisor, Dr. Wenlu Zhu for her guidance, support and patience over the course of my thesis. I am very grateful that I had the opportunity to work on this project with you because you always made sure I understood the material and took the time to explain it. You have made me a better scientist and critical thinker. I will forever cherish the memories I have of frantically emailing you when deadlines approached.

I would also like to thank James Bader for him always being there when I needed help. You helped me understand the material and went out of your way to assist me. I genuinely appreciate everything you did.

I also owe my gratitude to Zachary Zega, Geoun Ha, and Dr. Takamasa Kanaya for them always listening to my practice talks and providing me with much needed insightful feedback.

I also express my appreciation to Dr. Philip Piccoli and Dr. Michael N. Evans. Both of you have always been there for me during my time at UMD and thesis. Especially when I had statistics questions.

References

Bader, J., Zhu, W., Montesi, L., Cordonnier, B., Qi, C. and Kohlstedt, D. (2019) Anisotropic Permeability of Experimental Partially Molten Dunite Deformed in Shear. AGU Fall Meeting, San Francisco, CA

Bulau, J. R., Waff, H. S., & Tyburczy, J. A. (1979). Mechanical and thermodynamic constraints on fluid distribution in partial melts. Journal of Geophysical Research, 84(B11), 6102. https://doi.org/10.1029/jb084ib11p06102

Connolly, J. A. D., Schmidt, M. W., Solferino, G., & Bagdassarov, N. (2009). Permeability of asthenospheric mantle and melt extraction rates at mid-ocean ridges. Nature, 462(7270), 209–212. https://doi.org/10.1038/nature08517

Holtzman, B. K., Groebner, N. J., Zimmerman, M. E., Ginsberg, S. B., & Kohlstedt, D. L. (2003). Stress-driven melt segregation in partially molten rocks. Geochemistry, Geophysics, Geosystems, 4(5), n/a. https://doi.org/10.1029/2001gc000258

Kelemen, P. B., Hirth, G., Shimizu, N., Spiegelman, M., & Dick, H. J. (1997). A review of melt migration processes in the adiabatically upwelling mantle beneath oceanic spreading ridges. Philosophical Transactions of the Royal Society of London. Series A: Mathematical, Physical and Engineering Sciences, 355(1723), 283–318. https://doi.org/10.1098/rsta.1997.0010

King, D. S. H., Zimmerman, M. E., & Kohlstedt, D. L. (2009). Stress-driven Melt Segregation in Partially Molten Olivine-rich Rocks Deformed in Torsion. *Journal of Petrology*, *51*(1–2), 21–42. https://doi.org/10.1093/petrology/egp062

Kohlstedt, D. L., & Holtzman, B. K. (2009). Shearing Melt Out of the Earth: An Experimentalist's Perspective on the Influence of Deformation on Melt Extraction. Annual Review of Earth and Planetary Sciences, 37(1) ,561–593. https://doi.org/10.1146/annurev.earth.031208.100104

Kohlstedt, D. L., & Zimmerman, M. E. (1996). Rheology of Martially Molten Mantle Rocks. Annual Review of Earth and Planetary Sciences, 24(1), 41–62. https://doi.org/10.1146/annurev.earth.24.1.41

McKenzie, D. (1984). The Generation and Compaction of Partially Molten Rock. Journal of Petrology, 25(3), 713–765. https://doi.org/10.1093/petrology/25.3.713

Miller, K. J., Montési, L. G. J., & Zhu, W. (2015). Estimates of olivine–basaltic melt electrical conductivity using a digital rock physics approach. Earth and Planetary Science Letters, 432, 332–341. https://doi.org/10.1016/j.epsl.2015.10.004

Miller, K. J., Zhu, W., Montési, L. G. J., & Gaetani, G. A. (2014). Experimental quantification of permeability of partially molten mantle rock. Earth and Planetary Science Letters, 388, 273–282. https://doi.org/10.1016/j.epsl.2013.12.003

Qi, C., Hansen, L. N., Wallis, D., Holtzman, B. K., & Kohlstedt, D. L. (2018). Crystallographic Preferred Orientation of Olivine in Sheared Partially Molten Rocks: The Source of the "a-c Switch." Geochemistry, Geophysics, Geosystems, 19(2), 316–336. https://doi.org/10.1002/2017gc007309

Qi, C., Zhao, Y.-H., & Kohlstedt, D. L. (2013). An experimental study of pressure shadows in partially molten rocks. Earth and Planetary Science Letters, 382, 77–84. https://doi.org/10.1016/j.epsl.2013.09.004

Richardson, C. N., Lister, J. R., & McKenzie, D. (1996). Melt conduits in a viscous porous matrix. Journal of Geophysical Research: Solid Earth, 101(B9), 20423–20432. https://doi.org/10.1029/96jb01212

Spiegelman, M., & Kenyon, P. (1992). The requirements for chemical disequilibrium during magma migration. Earth and Planetary Science Letters, 109(3–4), 611–620. https://doi.org/10.1016/0012-821x(92)90119-g

Smith, C. S. (1964). Some elementary principles of polycrystalline microstructure. Metallurgical Reviews, 9(1), 1–48. https://doi.org/10.1179/mtlr.1964.9.1.1

Snow, D. T., (1965) A parallel-plate model of fractured permeable media, 331 pp., Ph.D. thesis, University of California, Berkeley

von Bargen, N., & Waff, H. S. (1986). Permeabilities, interfacial areas and curvatures of partially molten systems: Results of numerical computations of equilibrium microstructures. Journal of Geophysical Research 91(B9), 9261. https://doi.org/10.1029/jb091ib09p09261

Wark, D. A., & Watson, E. B. (1998). Grain-scale permeabilities of texturally equilibrated, monomineralic rocks. Earth and Planetary Science Letters, 164(3–4), 591–605. https://doi.org/10.1016/s0012-821x(98)00252-0

Zhu, W., Cordonnier, B., Qi, C. and Kohlstedt, D. (2017) Permeability and 3-D melt geometry in shear-induced high melt fraction conduits. AGU Fall Meeting, New Orleans, LA.

Zhu, W., Gaetani, G. A., Fusseis, F., Montesi, L. G. J., & De Carlo, F. (2011). Microtomography of Partially Molten Rocks: Three-Dimensional Melt Distribution in Mantle Peridotite. Science, 332(6025), 88–91. https://doi.org/10.1126/science.1202221

Zhu, Wenlu, & Hirth, G. (2003). A network model for permeability in partially molten rocks. Earth and Planetary Science Letters, 212(3–4), 407–416. https://doi.org/10.1016/s0012-821x(03)00264-4

Zimmerman, M. E., Zhang, S., Kohlstedt, D. L., & Karato, S. (1999). Melt distribution in mantle rocks deformed in shear. Geophysical Research Letters, 26(10), 1505–1508. https://doi.org/10.1029/1999gl900259

Honor Code:

I pledge on my honor that I have not given or received any unauthorized assistance on this assignment/examination.